This is the published version of the paper.

This version of the publication may differ from the final published version.

Permanent repository link: https://openaccess.city.ac.uk/id/eprint/26279/

Link to published version: http://dx.doi.org/10.1016/j.advengsoft.2021.103030
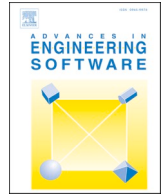
Analytical grid generation and numerical assessment of tip leakage flows in sliding vane rotary machines

Fanghua Ye [a,b], Giuseppe Bianchi [b,*], Sham Rane [c], Savvas A. Tassou [b], Jianqiang Deng [a,*]

[a] Shaanxi Key Laboratory of Energy Chemical Process Intensification, School of Chemical Engineering and Technology, Xi'an Jiaotong University, Xi'an 710049, China
[b] Institute of Energy Futures, Centre for Sustainable Energy Use in Food Chains, Brunel University London, Uxbridge, Middlesex UB8 3PH, United Kingdom
[c] Centre for Compressor Technology, City, University of London, 10 Northampton Square, London, EC1V 0HB, United Kingdom

ARTICLE INFO

ABSTRACT

The research presents a new analytical grid generation methodology for computational fluid dynamics studies in positive displacement sliding vane rotary machines based on the user defined nodal displacement approach. This method is more inclusive than state of the art ones since it enables the investigation of a broader range of design configurations, such as single, double and multiple-acting vane machines with non-circular housing, slanted blade and asymmetric blade tip profiles. Node number and radial divisions of blade tip are the parameters that affect most the mesh quality. The method was validated against indicated pressure measurements on a rotary vane expander resulting in a confidence interval within 4.31%. The benchmark analysis showed that the proposed method is as accurate as the manual ANSYS ICEM one but more than 1500 times faster (111s instead of 48h to generate 360 grids). The paper further proposes a novel method to track the leakage flows at the blade tip gaps of vane machines through a post-processing routine in ANSYS CFD-Post based on rotating monitoring planes. The leakage assessment on the vane expander case study showed that a 10 μm gap between blade tip and the 76 mm stator led to a 0.06 unit increase of the expander filling factor.

1. Introduction

Among the positive displacement machines, rotary vane ones benefit from simple geometry, low manufacturing complexity, compactness and competitive performance [1]. For these reasons, vane machines are currently employed in a broad range of industrial applications, such as refrigeration [2,3], compressed air [4,5], heat to power based on Organic Rankine Cycles (ORC) [6,7], desalination [8,9], automatic transmissions [10,11], as well as oil & gas [12].

The state of the art on rotary vane machinery research encompasses theoretical and experimental investigations. Regarding theoretical modelling, zero or one-dimensional (1D) formulations have been primarily employed [13,14]. The lower order formulations of conservation equations usually coupled with ideal gas assumptions undoubtedly reduce the computational cost. In turn, these simplified methods are suitable for optimisation studies [15]. Another key advantage of lumped parameter models is the easy integration of multi-physics phenomena, such as thermofluids and kinematics for the evaluation of friction losses [16]. On the other hand, the lack (0D) or low (1D) spatial resolution of the results does not thoroughly reflect the real complexity of the flow topology [17,18] and, in turn, hinders pathways to design optimisation.

Experimental research works have enabled performance assessments of rotary vane devices [19,20] and their systems [21,22]. Most of the experimental methodologies employed black-box setups, where the machine performance was evaluated through measurements at the inlet and the outlet ducts [2,23]. Some studies considered the installation of piezo-electric [22] or piezo-resistive [24] pressure transducers to retrieve the angular evolution of the pressure inside the vanes; this technique is commonly referred to as indicating measurement. To overcome the low spatial resolution of indicating pressure measurement techniques, some positive displacement machines have been investigated through the use of Particle Image Velocimetry (PIV) [25]. This methodology allows to retrieve planar velocity fields but involves substantial challenges to provide a suitable optical access to the pulsed laser beams. For these reasons, there are no PIV studies on vane machines.

The use of numerical simulation as a tool for research and design of rotary vane machines was therefore a breakthrough in this scientific field since it allowed to resolve complex flow topologies and gain insights towards optimised configurations. This was possible only after the development of algorithms that accurately discretised the moving and

---

* Corresponding authors.

E-mail addresses: giuseppe.bianchi@brunel.ac.uk, giuseppebianchiphd@gmail.com (G. Bianchi), dengjq@mail.xjtu.edu.cn (J. Deng).

deforming computational fluid domain of the working chambers, commonly referred to as rotor mesh. The most common grid generation methods based on the finite volume method to calculate the partial differential equations are spring smoothing, diffusion smoothing, layering, re-meshing and User Defined Nodal Displacement (UDND) [26]. Among these approaches, UDND methodology can be used to generate a series of node coordinates representing the rotor mesh at each time step externally, prior to the numerical flow solution. Hence, this methodology ensures space and equations conservation without any artificial sources [26]. To date, UDND methodology has been successfully employed to generate the computational mesh for vane machines and led to the development of two different algebraic strategies for grid generation.

In the first algebraic strategy, Spille-Kohoff et al. [27,28] developed a UDND approach that has been implemented in a commercial customised grid generation software named TwinMesh™. In this approach, after grid boundaries are imported from external files, the tool produces a set of two-dimensional (2D) rotor grids at each angular step including refined boundary layers towards rotor and stator walls. Afterwards, an iterative and explicit approach is used to smooth the grids to improve the mesh quality, i.e. orthogonality. The set of 2D grids are finally assembled to 3D grids and supplied to the CFD solver. As an application case, Lobsinger et al. [11] employed TwinMesh™ to generate the computational mesh for a double-acting rotary vane oil pump in automatic transmission systems of vehicles and carried out the CFD simulations with ANSYS CFX. The blade tip leakage as well as the cavitation characteristics were investigated in order to weaken cavitation and improve the pump efficiency. To reduce the computational cost, a 2D model instead of 3D model was selected. Besides rotary vane machines, this UDND methodology has also been successfully applied to twin-screw machines [28,29] and scroll machines [27]. However, to date, this methodology is exclusively available for numerical simulations with only ANSYS CFX as the CFD solver. Moreover, from the published literature, there is no evidence about the capability of this grid generation method to account for advanced geometrical features such as the blade offset or asymmetric blade tip profiles, which can be found in industrial vane machines, e.g. refrigeration compressors [30,31].

The second algebraic strategy was developed in the authors' earlier work [32] and it has been implemented in the Screw Compressor Rotor Grid Generator (SCORG™) software developed by PDM Analysis, a spin-off company of City, University of London. The UDND grid generation approach relies on algebraic algorithms with transfinite interpolation, post orthogonalisation and smoothing for internal nodes distribution. This method was experimentally validated against indicating pressure data on a rotary vane expander for ORC heat to power conversion applications [33]. Numerical studies were also carried out to assess the potential of supercharging the expander through a second intake line to increase the power output [24]. The validated simulation results showed that supercharging the expanders could increase the specific power output up to 2.4 times since overexpansion of the working fluid was avoided. However, this deforming grid generation methodology is only available for single-acting vane machines with circular stator profiles and blade centred configurations.

Besides the above two algebraic meshing methods, researchers also employed commercial meshing tools for grid generation for vane machines. Montenegro et al. [34] simulated a vane ORC expander with an elliptic stator with R245fa as working fluid based on OpenFOAM software. The rotor mesh was generated by the built-in Cartesian mesh tool in OpenFOAM. Rak et al. [35] also carried out numerical research on a vane ORC expander. To avoid the negative volumes of the rotor mesh, they decreased the blade thickness and increased the blade tip clearance gap. An embedded tool of ANSYS suite was used for the movement and deformation of the rotor mesh, which relocated the internal nodes based on a displacement diffusion model. Ye et al. [36] conducted two-phase simulations on a vane machine for desalination applications with ANSYS Fluent. A User Defined Function (UDF) was developed to control

the blade movement. The initial mesh generated by ICEM software deformed and reconstructed according to the boundary movement. However, the mesh had the disadvantage of a small number of grids (sometimes even one layer of grid) in the blade tip clearance gap, which may result in inaccurate simulation results.

To overcome all the shortcomings encountered in the above state-of-the-art research, this paper proposes a general grid generation methodology for rotary vane machines that is fully analytical and applicable to a broader range of rotary vane machine configurations such as multiple-acting chambers, non-circular stator, offset blade, asymmetric blade tip profile. After the development of this new grid generation method, a sensitivity analysis of the grid generation parameters on the mesh quality of an ORC vane expander was carried out to obtain the optimal mesh. Three-dimensional simulations were performed on the vane expander with ANSYS FLUENT as the solver. The simulation results were validated against the experimental indicating pressure data. Finally, a new post-processing routine was developed in ANSYS CFD-post software to obtain the blade tip leakage flows. The numerical results with analytical rotor mesh were compared to those with ICEM and differential rotor mesh.

2. Grid generation methodology

The analytical grid generation methodology of deforming domain (rotating part) in rotary vane machines includes: boundary generation, boundary discretisation, interior node distribution and coupling with the CFD solvers. The first three steps were carried out through a two-dimensional (2D) approach since the deforming domain has a constant cross section along the rotation axis. This 2D mesh of deforming domain is then assembled into 3D. Besides the deforming domain, the stationary domains including the two axial end leakage gaps and ports can be discretised through conventional meshing software such as ICEM or Gambit.

2.1. Boundary generation

A rotary vane machine consists of a rotating rotor with several slots machined at equal angular intervals along the rotor surface to host the blades. As the rotor rotates, the blades are expelled from the rotor, sliding along the slots toward the stator inner surface due to centrifugal force. This leads to periodically variable working chambers bounded by rotor, stator, blades and end wall plates.

In geometric terms, the rotor and stator are mounted with a given eccentricity (e), as shown in Fig. 1a-d. Based on the geometrical features, rotary vane machines can be classified into single-acting, double-acting and multiple-acting devices. As displayed in Fig. 1a and 1b, the single-acting machine has zero or one tangency region between rotor and stator, while the double-acting and multiple-acting devices have two or more tangency regions respectively, as illustrated in Fig. 1c and d. The rotor is always a circular cylinder to ensure rotodynamic balance, while the stator inner surface may have a non-circular cross section. Besides the circular curves, the stator profile can also accommodate elliptic curves, simple harmonic cures, polynomial curves, combination curves, etc. In Fig. 1e a vane machine geometry with a radial blade arrangement is shown. Fig. 1f relates to a blade-offset design configuration, where the blade centreline and the radial direction define the angle β_{bl}, named blade eccentric angle. As shown in Fig. 1g, the blade tip profile is usually symmetrical and circular. However, an asymmetrical blade tip profile can also be employed for rotary vane machines [37]. Similarly, a blade tip eccentric angle (β_{tip}) is proposed to account for this geometrical feature, as displayed in Fig. 1h.

The grid boundaries include rotor, stator and blade walls outside the rotor slots. Fig. 2 displays the calculation scheme of grid boundaries. As shown in Fig. 2a, the Cartesian coordinates of the rotor can be modelled as in Eq. (1):
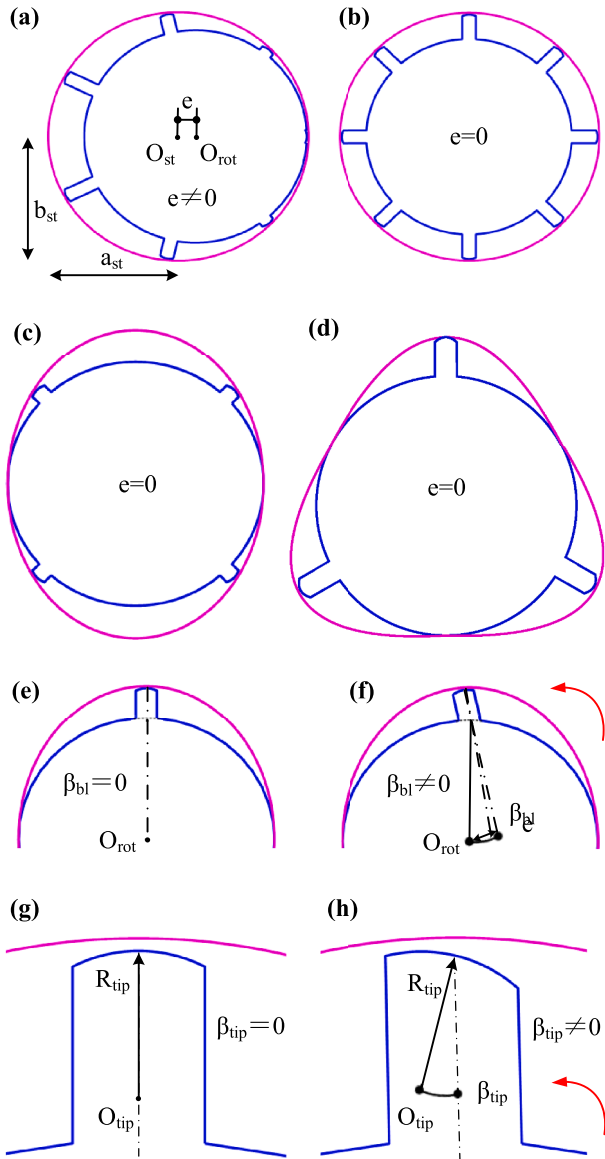
Fig. 1. Geometrical features of rotary vane machines: single-acting device with eccentric stator (a), single-acting device with centred stator (b), double-acting device (c), multiple-acting device (d); centred blade (e), eccentric blade (f); symmetrical blade tip profile (g), asymmetric blade tip profile (h).

$$\begin{cases} x_{rot} = R_{rot}\cos\theta \\ y_{rot} = R_{rot}\sin\theta \end{cases} \tag{1}$$

where θ is crank angle (rotor angle) and R_{rot} the rotor radius.

Unlike the always circular shape of the rotor, the stator profile may have a circular, elliptical or even irregular cross section. For instance, with reference to an elliptical configuration, the stator profile equation can be modelled as in Eq. (2):

$$\begin{cases} x_{st} = \dfrac{-b_{st}\left(eb_{st}\cos\varphi + a_{st}\sqrt{\left(a_{st}^2\sin^2\varphi + b_{st}^2\sin^2\varphi - e^2\sin^2\varphi\right)}\right)}{a_{st}^2\sin^2\varphi + b_{st}^2\sin^2\varphi}\cos\varphi \\[4mm] y_{st} = \dfrac{-b_{st}\left(eb_{st}\cos\varphi + a_{st}\sqrt{\left(a_{st}^2\sin^2\varphi + b_{st}^2\sin^2\varphi - e^2\sin^2\varphi\right)}\right)}{a_{st}^2\sin^2\varphi + b_{st}^2\sin^2\varphi}\sin\varphi \end{cases} \tag{2}$$

where φ is the stator angle, e the stator eccentricity, a_{st} and b_{st} the stator semi-axes. If a_{st} is equal to b_{st}, the elliptical stator profile becomes a circular one.
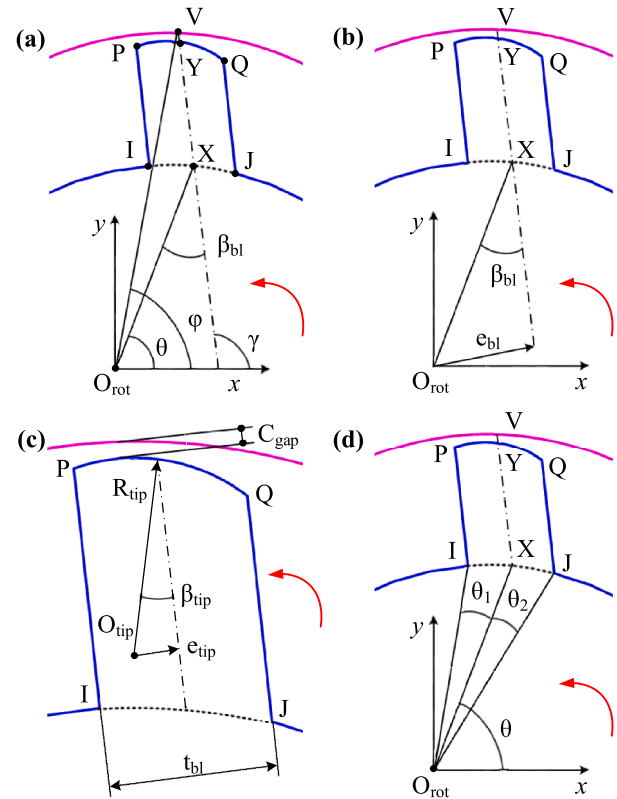
With reference to Figs. 2a and 2b, the relationship between the crank and stator angles can be expressed as in Eqs. (3) and (4):

$$\varphi = \theta + cos^{-1}\left(\frac{e_{bl}}{\sqrt{x_{st}^2 + y_{st}^2}}\right) - cos^{-1}\left(\frac{e_{bl}}{R_{rot}}\right) \tag{3}$$

$$e_{bl} = R_{rot}\sin\beta_{bl} \tag{4}$$

where e_{bl} is blade eccentricity, β_{bl} is blade eccentric angle.

The blade boundaries are defined through key points of the blade tip and side walls, namely the centre of circular tip profile (O_{tip}) and four endpoints (I, J, P and Q). The trajectories of these points depend on the blade tilt angle (γ) and the blade tip eccentricity (e_{tip}), shown in Figs. 2a and 2c respectively. These quantities are also defined in Eqs. (5) and (6).

$$\gamma = \theta + \beta_{bl} \tag{5}$$

$$e_{tip} = R_{tip}\sin\beta_{tip} \tag{6}$$

where R_{tip} is blade tip radius, β_{tip} is blade tip eccentric angle.

With reference to Fig. 2c, the centre of the circular blade tip profile can be calculated by Eq. (7):

$$\begin{cases} x_{otip} = x_{st} - \left(R_{tip} + C_{tip}\right)\cos\left(\gamma + \beta_{tip}\right) \\ y_{otip} = y_{st} - \left(R_{tip} + C_{tip}\right)\sin\left(\gamma + \beta_{tip}\right) \end{cases} \tag{7}$$

As illustrated in Fig. 2d, the rotor wall key points I and J can be calculated by Eqs. (8) and (9) respectively:

$$\begin{cases} x_I = R_{rot}cos(\theta + \theta_1) \\ y_I = R_{rot}sin(\theta + \theta_1) \end{cases} \tag{8}$$

Fig. 2. Geometrical parameters to define rotary vane machines: relationship between crank angle θ and stator angle φ (a), blade eccentric angle β_{sta} (b), blade tip eccentric angle β_{tip} (c), angles to define blade side walls (d).

circular one.

$$\begin{cases} x_J = R_{rot}cos(\theta - \theta_2) \\ y_J = R_{rot}sin(\theta - \theta_2) \end{cases} \tag{9}$$

where θ_1 and θ_2 can be respectively calculated by Eqs. (10) and (11):

$$\theta_1 = cos^{-1}\left(\frac{e_{bl} - t_{bl}/2}{R_{rot}}\right) - \left(\frac{\pi}{2} - \beta_{bl}\right) \tag{10}$$

$$\theta_2 = \left(\frac{\pi}{2} - \beta_{bl}\right) - cos^{-1}\left(\frac{e_{bl} + t_{bl}/2}{R_{rot}}\right) \tag{11}$$

Another two key points P and Q on the blade tip wall can be calculated by Eqs. (12) and (13) respectively:

$$\begin{cases} x_P = x_{otip} + R_{tip}cos\left(\gamma + sin^{-1}\dfrac{t_{bl}/2 - e_{tip}}{R_{tip}}\right) \\ y_P = y_{otip} + R_{tip}\ sin\left(\gamma + sin^{-1}\dfrac{t_{bl}/2 - e_{tip}}{R_{tip}}\right) \end{cases} \tag{12}$$

$$\begin{cases} x_Q = x_{otip} + R_{tip}cos\left(\gamma - sin^{-1}\dfrac{t_{bl}/2 + e_{tip}}{R_{tip}}\right) \\ y_Q = y_{otip} + R_{tip}\ sin\left(\gamma - sin^{-1}\dfrac{t_{bl}/2 + e_{tip}}{R_{tip}}\right) \end{cases} \tag{13}$$

With the obtained key points, the blade tip wall (PQ) and blade side walls (IP and JQ) can be respectively generated through Eqs. (14-16):

$$\begin{cases} x_{PQ} = x_{otip} + R_{tip}cos(\gamma + \delta_1) \\ y_{PQ} = y_{otip} + R_{tip}sin(\gamma + \delta_1) \end{cases},$$

$$-sin^{-1}\frac{t_{bl}/2 + e_{tip}}{R_{tip}} \le \delta_1 \le sin^{-1}\frac{t_{bl}/2 - e_{tip}}{R_{tip}} \tag{14}$$

$$\begin{cases} x_{IP} = x_I + \delta_2 cos\gamma \\ y_{IP} = y_I + \delta_2 sin\gamma \end{cases},$$

$$0 \le \delta_2 \le \sqrt{(x_p - x_I)^2 + (y_p - y_I)^2} \tag{15}$$

$$\begin{cases} x_{JQ} = x_J + \delta_3 cos\gamma \\ y_{JQ} = x_J + \delta_3 sin\gamma \end{cases},$$

$$0 \le \delta_3 \le \sqrt{(x_Q - x_J)^2 + (y_Q - y_J)^2} \tag{16}$$

Since the minimum gap between the stator wall and blade tip wall occurs only once considering the finite blade thickness, an adjustment is needed to perform the inwards or outwards translation of the blade along its slot, as displayed in Fig. 3. If the minimum blade tip gap is higher than its input value, an outwards translation of the blade along its slot is performed for correction. On the other hand, an inwards translation occurs when the minimum blade tip gap is lower than its input value. It should be noted that if the blade eccentric angle is equal to zero,
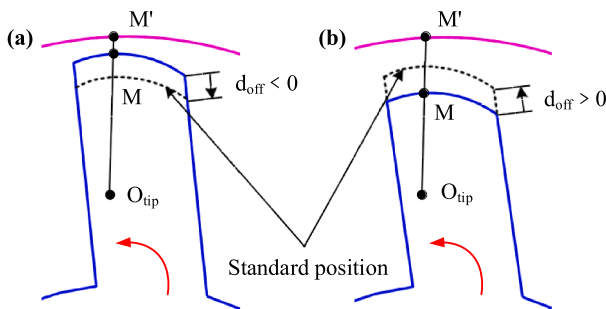
the inwards or outwards translation is along the radial direction. Otherwise, a new general equation needs to be developed to calculate the offset magnitude along the blade slot according to Eq. (17).

$$d_{off} = min\left(\sqrt{(x_{M'} - x_M)^2 - (y_{M'} - y_M)^2}\right) - C_{gap} \tag{17}$$

where d_{off} is offset magnitude, M is any point on the blade tip wall, M'is the corresponding point on the stator wall. These two points are collinear with the centre of the circular tip profile.

2.2. Boundary discretisation and node distribution

The fully analytical approach allows to use an "O" topology for the rotor mesh. Division lines (II', JJ', PP', QQ' and KK') are proposed to divide the "O" domain into three types of region: core region, blade side region and blade tip region, as shown in Fig. 4. An eccentric angle of the regional division line, $\Delta\gamma$, defines the division lines. PP' and QQ' are parallel to II' and JJ' respectively. The stator wall is therefore divided into multiple segments I'K', I'P', P'Q' and J'Q' that correspond to rotor wall IK, blade side wall IP, blade tip wall PQ and blade side wall JQ respectively.

The index notations for the boundary discretisation and node distribution procedure refer to the scheme displayed in Fig. 5. Here$r_{i,j}(x, y)$ represents the points on the boundary profiles in terms of the physical coordinate system, where r is nodal radius vector, index i is along the circumferential direction of the boundary profile (composed of the blade tip wall, blade side wall, rotor wall together with the stator wall) and index j is along the radial direction of the mesh line. A value of $i = 1$ indicates the first node on the boundary profile while $i = I$ is the last node. I is the total number of nodes used to discretise a particular boundary curve. Index $j = 1$ indicates the rotor boundary (composed of rotor walls, blade side walls and blade tip walls) and $j = J$ indicates the stator boundary (stator wall). J is the total number of nodes in the radial direction.

2.2.1. Core region

The discretisation of the core region is illustrated in Fig. 6. The inner boundary is the rotor wall IK and the outer boundary is the corresponding stator wall segment I'K', as shown in Fig. 6a. The nodes on the inner boundary outer boundaries are uniformly distributed according to their arc length based on Eqs. (18) and (19) respectively:

$$\left|r_{i+1,\ j=1}(x, y) - r_{i,\ j=1}(x, y)\right| = \left|r_{i,\ j=1}(x, y) - r_{i-1,\ j=1}(x, y)\right| \tag{18}$$

$$\left|r_{i+1,\ j=J}\ (x, y) - r_{i,\ j=J}(x, y)\right| = \left|r_{i,\ j=J}(x, y) - r_{i-1,\ j=J}(x, y)\right| \tag{19}$$

where $i = 2, 3, 4\ldots(N_{rot} - 1)$, N_{rot} is the number of the nodes on the rotor wall.

Fig. 3. Schematic of the blade offset along its slot: inwards translation (a), outwards translation (b).
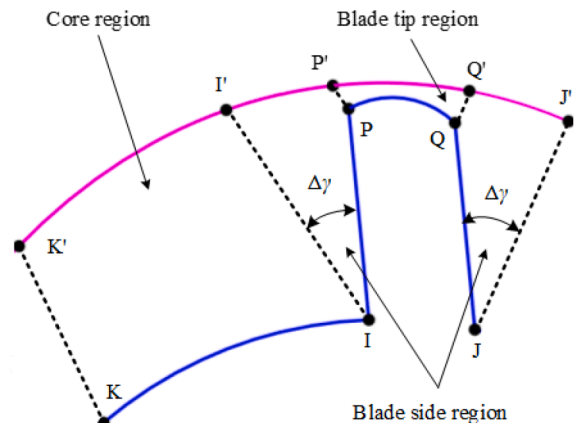

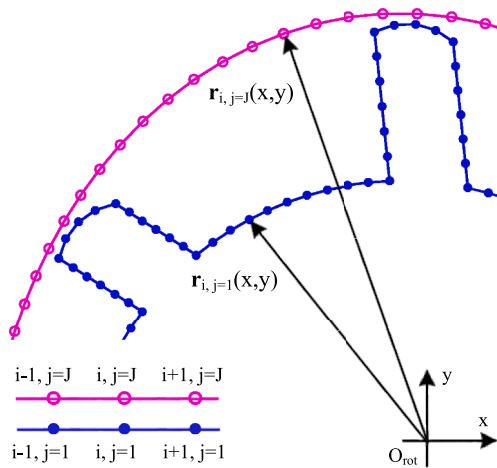**Fig. 4.** Regional division of rotor fluid domain.

Fig. 5. Reference scheme for nodal radial vector.

Fig. 6. Core region discretisation: boundary generation (a), discretisation of inner and outer boundaries (b), connection between inner and outer boundary nodes (c), internal node distribution (d).

Fig. 6b displays the resultant node distribution with 10 nodes on the rotor wall IK and stator wall I'K'. The next step is the connection process between the nodes on the rotor wall and the corresponding stator wall, as shown in Fig. 6c. After that, all connection lines are respectively divided into equidistant radial divisions (seven divisions are shown in Fig. 6d) for interior node distribution.

2.2.2. Blade side region

As shown in Fig. 7a, the blade side walls (IP and JQ) are parallel surfaces that form a convex connection with the blade tip wall (PQ). This convexity is a big challenge for generating high-quality mesh because the aspect ratio between the core and blade tip regions changes by many orders of magnitude. Therefore, a stretching function is applied on the blade side walls in order to gradually flare the radial mesh lines from blade tip region into the core region, which concentrates the nodes towards the blade tip region while increasing the node spacing close to the rotor wall. A stretching parameter σ_{side} is introduced on the blade side walls (IP and JQ) and the corresponding stator wall segments (I'P' and J'Q') according to Eqs. (20) and (21) respectively.

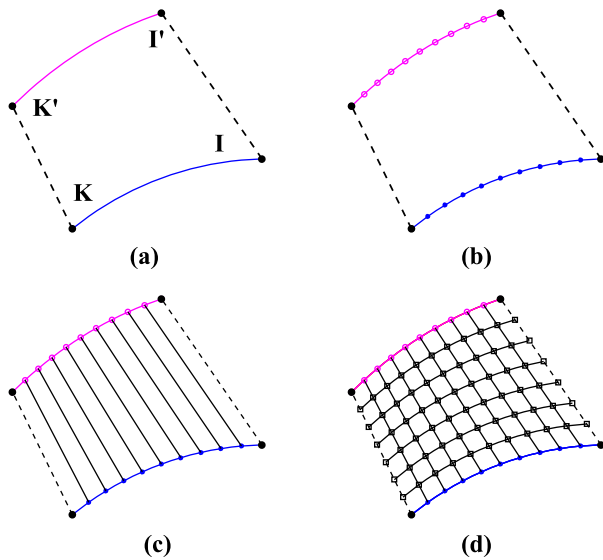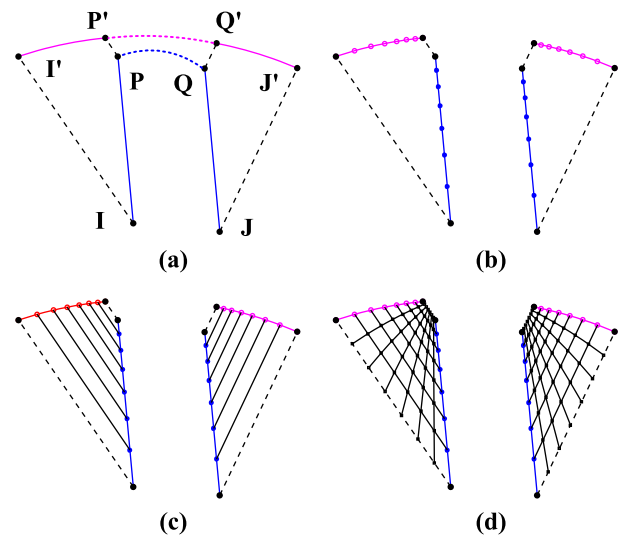**Fig. 7.** Blade side region discretisation: boundary generation (a), discretisation of inner and outer boundaries (b), connection between inner and outer boundary nodes (c), internal node distribution (d).

$$\left| \boldsymbol{r}_{i+1,\,j=1}(x,y) - \boldsymbol{r}_{i,\,j=1}(x,y) \right| = \sigma_{side}\left(\left| \boldsymbol{r}_{i,\,j=1}(x,y) - \boldsymbol{r}_{i-1,\,j=1}(x,y) \right| \right) \quad (20)$$

$$\left| \boldsymbol{r}_{i+1,\,j=J}(x,y) - \boldsymbol{r}_{i,\,j=J}(x,y) \right| = \sigma_{side}\left(\left| \boldsymbol{r}_{i,\,j=J}(x,y) - \boldsymbol{r}_{i-1,\,j=J}(x,y) \right| \right) \quad (21)$$

where $i = 2, 3, 4 \ldots (N_{side} - 1), 0.1 \leq \sigma_{side} \leq 1$, N_{side} is the number of the nodes on the blade side walls.

The resultant node distribution with 8 nodes on the blade side wall and $\sigma_{side} = 0.85$ is highlighted in Fig 7b. Similarly to the core region, later steps are the connection between the nodes on the blade side walls (IP and JQ) and the corresponding stator wall segment (I'P' and J'Q'), as seen in Fig. 7c. Finally, all connection lines are respectively divided into equidistant radial divisions for interior node distribution (see Fig. 7d).

At the tangency region between the rotor and stator, the nodes on the blade side walls (IP and JQ) would be fairly dense due to the short length of blade side walls, thus potentially leading to poor grid quality or even computational divergence. Therefore, a small geometrical simplification was introduced to convert the blade side wall into a short segment on the rotor surface, as shown in Fig. 8. It should be noted that this geometrical simplification of the blade side wall does not affect leakage flow as the tip clearance gap does not change. Regardless of the blade sliding outside (Fig. 8a) or inside the rotor (Fig. 8b), the simplification with an offset angle ζ_{off} was introduced on the blade side wall when its length
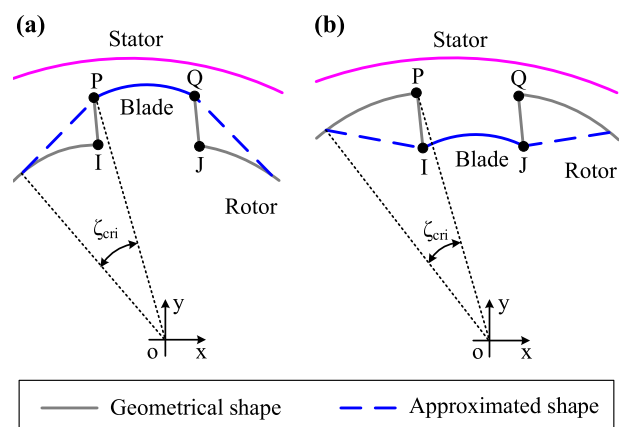

Fig. 8. Simplification at the tangency region: blade slides outside rotor (a), blade slides inside rotor (b).

was smaller than a critical simplification threshold (L_{cri}). This critical value was determined by Eq. (22):

$$L_{cri} = R_{rot}\xi_{cri} \qquad (22)$$

where ζ_{cri} is critical simplification angle.

2.2.3. Blade tip region

The discretisation of the blade tip region is displayed in Fig. 9. The blade tip wall PQ is the inner boundary and the corresponding stator wall segment P'Q' is the corresponding outer boundary, as shown in Fig. 9a. The nodes are uniformly distributed on the blade tip wall PQ according to Eq. (18), where $i = 2, 3, 4...N_{tip} - 1$, N_{tip} is the number of the nodes on the blade tip wall. The arc length values of the blade tip wall PQ and the stator wall segment P'Q' are not equal, thus potentially leading to poor grid orthogonality. Therefore, another stretching function is introduced on the stator wall segment P'Q' to improve the grid orthogonality. This function concentrates the nodes close to both ends of the P'Q' and increases the node spacing in the middle of this segment. Equidistance distribution is modified using a stretching parameter σ_{tip} according to Eqs. (23) and (24).

$$\left|\boldsymbol{r}_{i+1, \, j=J}(x,y) - \boldsymbol{r}_{i, \, j=J}(x,y)\right| = \sigma_{tip}{}^{k}\left|\boldsymbol{r}_{i, \, j=J}(x,y) - \boldsymbol{r}_{i-1, \, j=J}(x,y)\right|, \qquad (23)$$

$$k = \begin{cases} 1, & i < \left(1 + N_{tip}\right)/2 \\ 0, & i = \left(1 + N_{tip}\right)/2 \\ -1, & i > \left(1 + N_{tip}\right)/2 \end{cases} \qquad (24)$$

where $i = 2, 3...N_{tip} - 1$, $0.1 \leq \sigma_{tip} \leq 1$.

Fig. 9b shows the resultant node distribution with 11 nodes on the stator wall segment P'Q' and $\sigma_{tip} = 0.99$. Similar to the core region and the blade side region, the next step is the connection between the nodes on the blade tip wall PQ and the corresponding stator wall segment P'Q', as shown in Fig. 9c. With the equidistant node distribution in the radial direction, the internal node distribution is illustrated in Fig. 9d.

2.3. Coupling with commercial CFD solvers

Fig. 10 summarises all the numerical steps of CFD simulations with the newly proposed analytical grid generation methodology. All parameters for geometry, boundary discretisation and node distribution need to be prescribed at the onset. Table 1 displays sample inputs of the main parameters for the vane expander test case. After the boundary generation, boundary discretisation and interior node distribution mentioned above, the 2D mesh is generated for all time steps, representing a full rotation of the rotor. The grids are then assembled into 3D mesh for the first position (baseline mesh) in the solver. The analytical grid generation procedure yields a grid database consisting of node coordinates for all time steps. This information is stored in a series of data files read by the CFD solver as the mesh is updated with time.
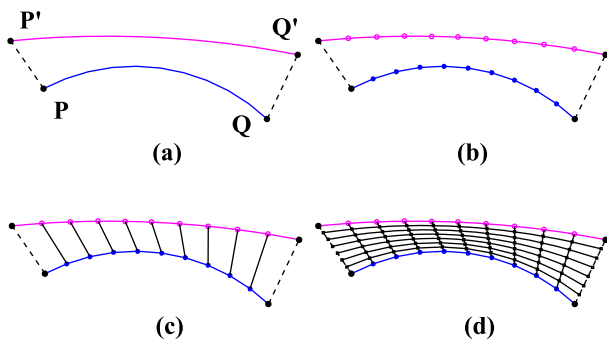
Fig. 9. Blade tip region discretisation: boundary generation (a), discretisation of inner and outer boundaries (b), connection between inner and outer boundary nodes (c), internal node distribution (d).
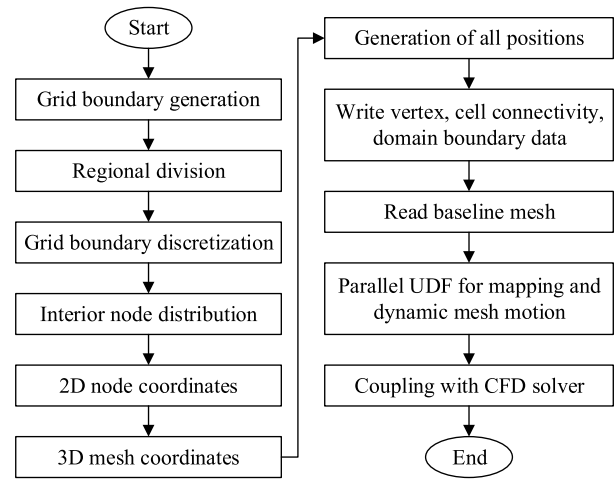
Fig. 10. Flow chart for analytical grid generation coupling with CFD solvers.

Table 1
Geometric parameters of the rotary vane expander.

Quantity	Value	Unit
Number of blades	7	-
Rotor radius	32.50	mm
Stator x semi axis	38.00	mm
Stator y semi axis	38.00	mm
Eccentricity	5.45	mm
Axial length	60.00	mm
Blade thickness	3.96	mm
Blade tip radius	4.25	mm
Blade tip clearance	0.01	mm
Blade eccentric angle	0	°
Blade tip eccentric angle	0	°
Main intake port opening angle	4.4	°
Main intake port closing angle	48.0	°
Second intake port opening angle	93.2	°
Second intake port closing angle	106.8	°
Outlet port opening angle	180	°
Outlet port closing angle	320	°

The next stage of CFD simulations is the coupling of the generated mesh dataset with the commercial solver. The detailed coupling method is reported in the authors' previous work [32] while the parallelisation of the User Defined Function (UDF) for the FLUENT solver is thoroughly explained in [38]. Once the initial mesh is loaded in FLUENT, at the first time step, the parallel UDF performs a mapping procedure to find a unique correspondence between mesh nodes and node coordinates stored in the data files resulting from the grid generation. Afterwards, the same UDF is employed to read the node coordinates in the data files and update the mesh at every time step. Finally, the rotor mesh is connected to stationary fluid domains, e.g. ports, by non-conformal interfaces.

3. Sensitivity analysis of mesh quality

Mesh quality is crucial to ensure calculation stability and to obtain accurate results. A sensitivity analysis of the grid generation parameters on the mesh quality was performed with reference to an ORC rotary vane expander, whose geometrical features are listed in Table 1. The ranges of the ten independent grid generation parameters for the sensitivity analysis of the rotor mesh quality are presented in Table 2. The four indicators used to evaluate the mesh quality are: maximum aspect ratio, maximum expansion factor, minimum orthogonality quality and minimum skewness quality.

Fig. 11 shows the effects of grid generation parameters on the node count and the mesh quality indicators. The total node number increased

Table 2

Ranges for independent variables of mesh quality sensitivity analysis.

Grid generation parameters	Min			Ref			Max
Node number on blade tip wall (N_{tip})	9	13	17	21	25	29	33
Stretching parameter on blade tip wall (σ_{tip})	0.94	0.95	0.96	0.97	0.98	0.99	1.00
Node number on blade side wall (N_{side})	4	6	8	10	12	14	16
Stretching parameter on blade side wall (σ_{side})	0.70	0.75	0.80	0.85	0.90	0.95	1.00
Node number on rotor outer wall (N_{rot})	9	13	17	21	25	29	33
Node number in the radial direction (N_{rad})	5	6	7	8	9	10	11
Node number in the axial direction (N_{axi})	35	40	45	50	55	60	65
Offset angle of regional division line ($\triangle\gamma$)	15°	20°	25°	30°	35°	40°	45°
Critical angle for simplification (ζ_{cri})	0.1°	0.4°	0.7°	1.0°	1.3°	1.7°	1.9°
Offset angle for simplification (ζ_{off})	0.1°	0.4°	0.7°	1.0°	1.3°	1.6°	1.9°

drastically with the number of the radial and axial nodes (Fig. 11a). Therefore, these two parameters need to be carefully selected due to the impact on the computational resources and time.

Increasing the number of radial nodes (N_{rad}) led to higher aspect ratio (Fig. 11b) and worse orthogonality quality (Fig. 11d). However, too low value would result in inaccurate simulation results. Therefore, 8 radial nodes were selected for the present case.

A larger node number in the axial direction (N_{axi}) helped to lower the grid expansion factor, as displayed in Fig. 11c. Taking both mesh quality and cell count into account, 50 axial nodes were recommended for the expander.

Increasing the number of nodes on the blade tip wall (N_{tip}) contributed to better orthogonality quality (Fig. 11d), but also led to higher aspect ratio (Fig. 11b) and worse skewness quality (Fig. 11e). With reference to the overall impact on the mesh quality, 21 nodes on the blade tip wall were selected.

The node number on the blade side wall (N_{side}) also had a significant impact on the maximum expansion factor. As shown in Fig. 11c, the maximum expansion factor decreased as the blade side node number increased from 4 to 8, and then increased as the blade side node number increased from 8 to 16. Hence, 8 nodes on the blade side wall were assumed to be acceptable.

A larger node number on the rotor wall (N_{rot}) helped to lower the maximum expansion factor (Fig. 11c), but with no effects on the grid aspect ratio (Fig. 11b), orthogonality (Fig. 11d) and skewness (Fig. 11e). In order to keep the total number of cells of the computational mesh to a minimum, 21 nodes on the rotor wall were considered to be acceptable.

Although the other five grid generation parameters had no effect on the node count (Fig. 11a), they influenced the mesh quality in different aspects (Figs. 11b-11e). As shown in Fig. 11d and 11e, the grid orthogonality and skewness were sensitive to the stretching parameter on the stator wall segments which corresponded to the blade tip walls (σ_{tip}). A slight stretch with this value of 0.99 helped to obtain the best mesh quality.

On the other hand, the stretching parameter on the blade side walls and the corresponding stator wall segments (σ_{side}) also influenced the grid expansion factor, as shown in Fig. 11c. The value of 0.8 helped to gradually flare the radial mesh lines from the blade tip region to the core region.

Increasing the eccentric angle of the regional division line ($\triangle\gamma$) from 15° to 45° resulted in low aspect ratios and expansion factors as well as high orthogonality and skewness of the grid. Therefore, 45° is selected for this eccentric angle.

With a low critical angle for the blade side wall simplification (ζ_{cri}), the geometrical simplification would not be carried out, leading to high grid expansion factor, as shown in Fig. 11c. From the results, 1° is recommended for this critical angle.

Fig. 11c also shows that an offset angle for the blade side wall simplification (ζ_{off}) higher than 0.4° helped to control the grid expansion factor. However, large offset angles should be avoided since they would change the shape of the upstream and downstream regions of the tip leakage gap. Therefore, a 0.7° offset angle was selected for the expander.

In conclusion, the parameters that mostly affected the grid quality are number and radial divisions of blade tip. Table 3 further summarises the outcomes of the sensitivity study and compares the mesh quality of the baseline and optimal grid generation parameters. The parameter improvements contributed to better mesh quality even with less grid cell count.

4. Simulations setup

The optimal rotor mesh and the ports mesh of the ORC expander are shown in Fig. 12. The test case refers to a supercharged expander, i.e. with two suction lines, as displayed in Fig. 12e. The rotor mesh was generated by the developed analytical grid generation methodology, while the port fluid domains were discretized using tetrahedral mesh by ANSYS Meshing software. Table 4 shows the port mesh quality. The cell count for all port domains was 261696. Experimental values for rotational speed, pressures and temperatures at the inlet and the outlet sections of the machine, listed in Table 5, were used as boundary conditions.

As displayed in Fig. 12, the suction process occurred through two radial ports: main inlet and second inlet (supercharging port), while the discharge ports were located on the two end walls of the rotor fluid domain. The non-conformal sliding interfaces along the stator surface was used for mass and energy exchange between inlet ports and rotor domain, while the interface on the end wall plates was used for mass and energy exchange between outlet ports and rotor domain.

The working fluid was R245fa in the present study. The Aungier Redlich Kwong real gas model was employed to develop the coefficients of the polynomials to define R245fa properties and equation of state [39]. In this work, a four-order polynomial for the specific heat of R245fa was developed in Eq. (27). The critical state pressure 36.51 bar and the critical state temperature 427.16 K were provided to establish a lookup table in the pressure range from 2.00 to 60.00 bar, while the temperature range was between 273.0 and 400.0 K. Though this equation is a function of temperature, the coefficients are zero pressure, ideal gas coefficients obtained from REFPROP and the solver internally uses an energy integration procedure in each computational cell to get the specific heat data varying with pressure as well as temperature [39].

$$C_p^0(T) = 1.149 \times 10^2 + 3.536T - 5.174 \times 10^{-3}T^2 + 6.958 \times 10^{-6}T^3$$
$$- 4.261 \times 10^{-9}T^4$$

(27)

Detailed settings on FLUENT solver are presented in Table 6. The full rotor revolution was defined by 360 grid positions, leading to an angular step of 1°. Therefore, at a rotational speed of 1515 RPM, the time step was equal to 1.100×10^{-4} s. Three full rotor revolutions were considered in the present analysis, leading to 1080 time steps and a periodic flow solution. All CFD simulations ran on a PC with i7-6700 CPU at 3.40GHz. Four cores were employed while the RAM usage was 6.6 GB. The parallel simulation run in double precision required around 34 h to complete the simulation of three full revolutions of the expander.

5. Experimental validation

To validate the novel analytical grid generation method, the numerical results of the indicating pressure trace have been compared with
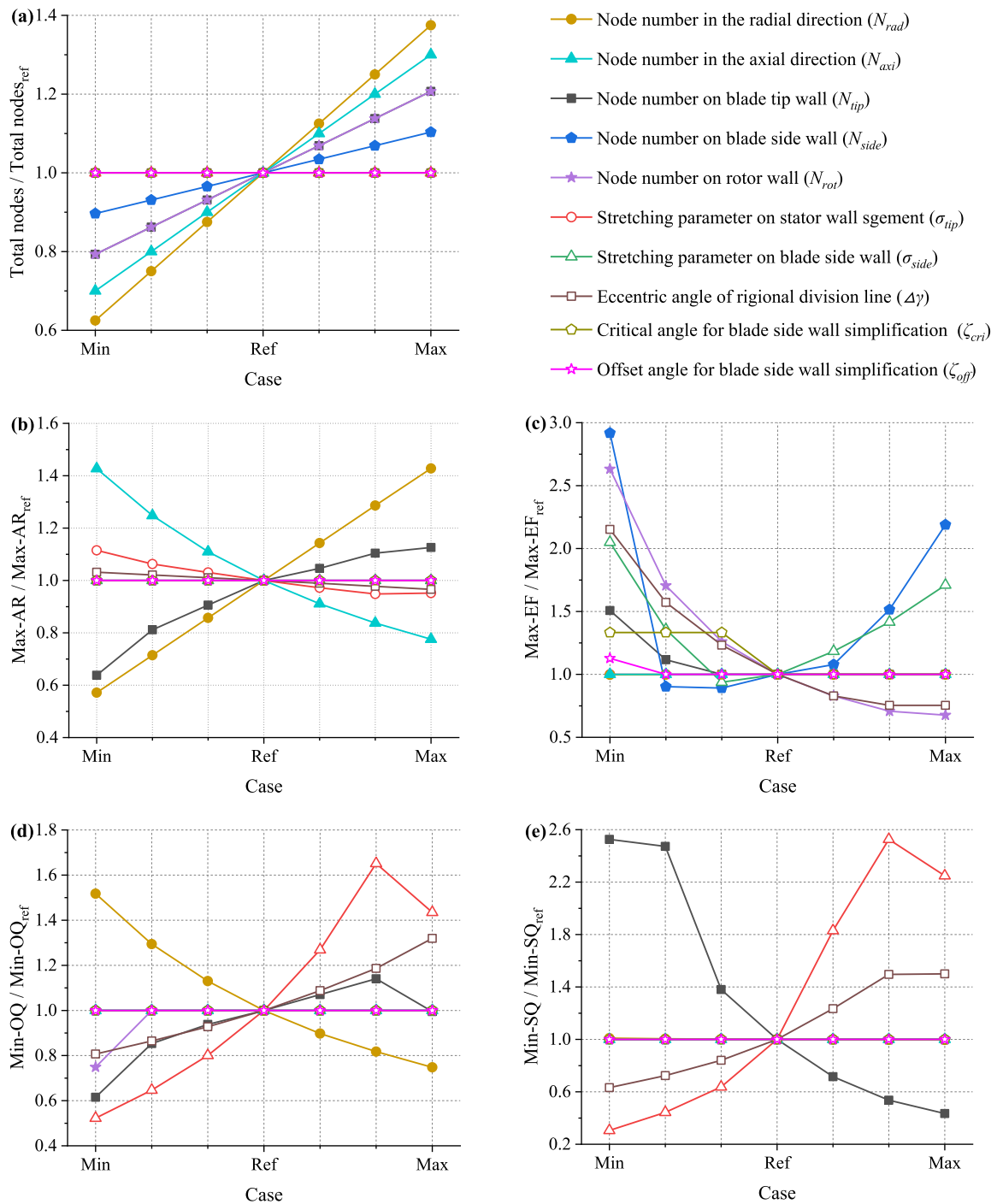
Fig. 11. Impact of the grid generation parameters on mesh quality: number of total nodes (a), maximum aspect ratio (Max-AR) (b), maximum expansion factor (Max-EF) (c), minimum orthogonality quality (Min-OQ) (d), minimum skewness quality (Min-SQ) (e).

the corresponding experimental data [24]. In the simulation, a series of monitoring points were foreseen to retrieve the internal pressure, while in the experiment three piezo-resistive pressure transduces were used to measure the cell pressure values. Fig. 13 shows the comparison of the internal pressure between the simulated and experimental results. The pressure values were in good agreement, given the modelling simplification (e.g., no leakage at the end wall plates). The experimental pressure value before 45° remained constant since it was not measured by the piezo-resistive transducers, but by a low frequency pressure transducer at the inlet duct. This pressure value was used to set up the inlet

boundary condition of the simulations. After 45°, the simulated and experiment pressure traces followed a very similar trend. The error between experimental and simulated pressures was within a 4.3% confidence interval. This outcome allows to retain the quantitative validation of the proposed analytical grid generation methodology as satisfactory.

Table 7 presents a summary of the numerical and experimental performance of the rotary vane expander. The simulated mass flow rates at both main and second intake ports were respectively lower than the experimental ones. This was because the expander was overfilled. The additional flow rate did not produce mechanical work but was

Table 3
Summary of the sensitivity analysis on mesh quality.

Grid generation parameters	Baseline	Optimal
Node number on blade tip wall (N_{tip})	21	21
Stretching parameter on blade tip wall (σ_{tip})	10	8
Node number on blade side wall (N_{side})	21	21
Stretching parameter on blade side wall (σ_{side})	8	8
Node number on rotor outer wall (N_{rot})	50	50
Node number in the radial direction (N_{rad})	0.85	0.80
Node number in the axial direction (N_{axi})	0.97	0.99
Offset angle of regional division line ($\Delta\gamma$)	30°	45°
Critical angle for simplification (ζ_{cri})	1.0°	1.0°
Offset angle for simplification (ζ_{off})	1.0°	0.7°
Total nodes of rotor mesh	162400	151200
Total cells of rotor mesh	139258	129654
Maximum aspect ratio	788.783	753.469
Maximum expansion factor	9.832	6.877
Minimum orthogonality quality	0.056	0.077
Minimum skewness quality	0.140	0.247

laminated through the clearance gaps (like the end face clearance and rotor slots) that have not been considered in the CFD modelling. This explain the mass flow rate mismatching. The lower value of the numerical outlet temperature is instead justified by the assumption of adiabatic walls. The lower experimental torque value was due to the actual mechanical power measurement in the experiment. In fact, the friction losses were not considered in CFD results. Therefore, the ratio of the experimental torque value to the simulated ones in this work can be used to estimate the mechanical efficiency of the vane expander. The obtained mechanical efficiency of 65.7% was very encouraging compared to other positive displacement expanders [40,41].

6. Results and discussions

This section reports a comparison between simulation results obtained through different rotor grid generation approaches. The purpose of this assessment is to show the improvement with respect to the state of the art as well as the impact of the grid generation method on the vane machine performance.

Another innovative aspect of this research is the numerical computation of the leakage flow at the blade tip of rotary vane machines. In fact, this clearance gap has a crucial impact on the volumetric efficiency, i.e. the filling factor in the case of expanders. To better appreciate the tip leakage flow in the case of a standard vane machine, the second inlet port was discarded.

All simulations were carried out with reference to the same port meshes (see Fig. 12), and the same settings in the FLUENT solver (see Table 5). The different rotor grids referred to the same geometrical parameters (Table 1) but resulted from: manual grid generation in ANSYS ICEM for each rotor position; the current analytical methodology; differential grid generation method according to [42]. The ICEM grid is the

Table 4
Mesh quality of inlet and outlet ports.

Mesh quality	Main inlet port	Second inlet port	Outlet port
Maximum aspect ratio	17.993	5.488	17.636
Maximum expansion factor	6.656	4.849	9.665
Minimum orthogonality	0.064	0.617	0.151
Minimum skewness	0.440	0.604	0.212
Total cell count	59703	12260	189733

Table 5
Experimental boundary conditions with measurement uncertainty [24].

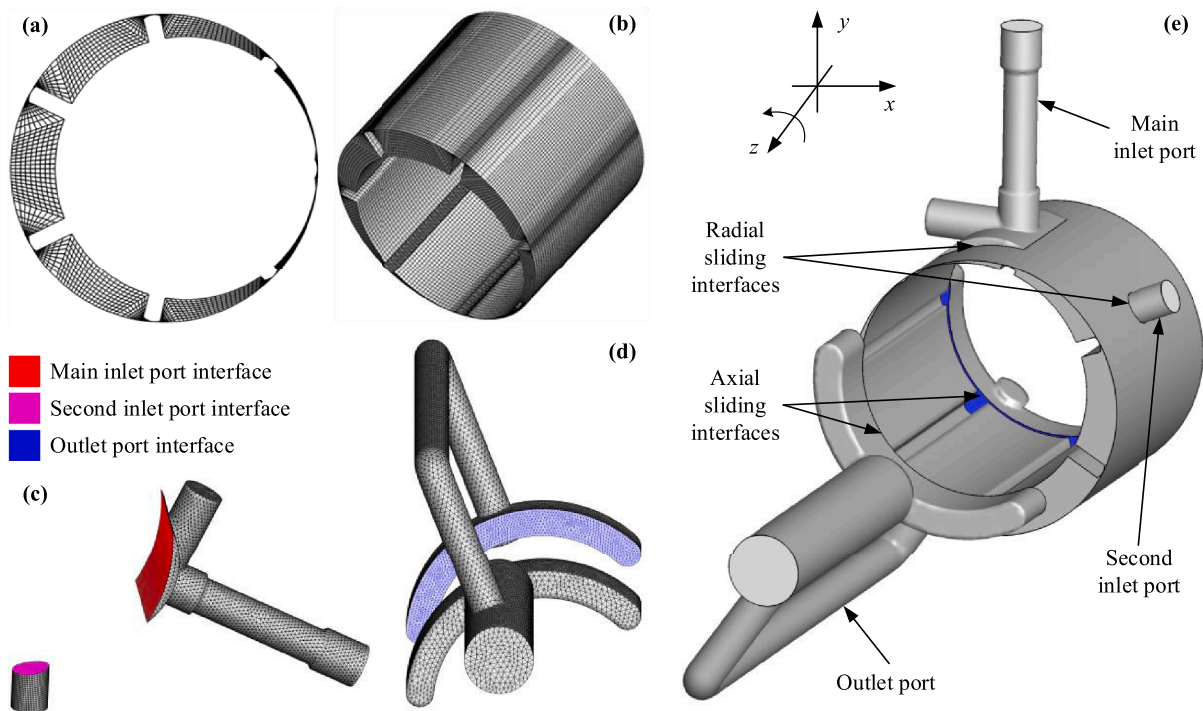|	Pressure ± 0.3 bar	Temperature ± 0.3 °C	Rotation speed ± 1 rpm
Main inlet	5.44	94.3	1515
Second inlet	4.74	94.3	
Outlet	3.21	85.9	

Fig. 12. CFD model of the vane expander with supercharged inlet: 2D rotor mesh (a), 3D rotor mesh (b), inlet ports meshes (c), outlet port mesh (d), assembled model (e).

Table 6
Detailed settings in ANSYS Fluent solver.

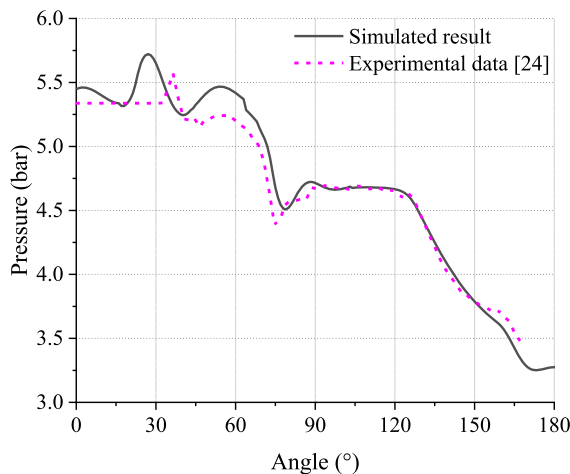| Criteria	Specification	Setting or value
Solver type	Pressure-based	-
Physical properties	R245fa	Aungier Redlich Kwong real gas model
Model selection	Turbulence model	SST k-ω
Solution methods	Pressure-velocity coupling	Coupled
	Control volume gradients	Least squares cell based
	Spatial discretisation	Pressure: standard
		Density: first order upwind
		Momentum: first order upwind
		Turbulent kinetic energy: first order upwind
		Specific dissipation rate: first order upwind
		Energy: first order upwind
	Transient formulation	First order implicit
Solution controls	Flow courant number	2
	Explicit relaxation factors	0.25
	Under-relaxation factors	0.1
	Convergence criteria	0.001
	Angular step size	1°
	Number of time steps	1080
	Max iterations per time step	100

Fig. 13. Comparison between simulated and experimental results in terms of angular pressure trace.

Table 7
Summary of the simulated and experimental performance of the expander.

Items	Simulated result	Experimental data [24]
Main inlet mass flow rate (g/s)	24	61 ± 0.15%
Second inlet mass flow rate (g/s)	33	39 ± 0.05%
Outlet temperature (°C)	83.7	85.9 ± 0.3
Rotor torque (Nm)	3.12	2.05 ± 0.02
Specific power (W/(g/s))	8.66	3.25
Estimated mechanical efficiency	65.7%	

benchmark since this method required no geometrical simplification at the tangency region. From here onwards, reference to the three rotor grids will be respectively made through the following abbreviations: ICEM, analytical, differential.

6.1. In-cell angular pressure evolution

Fig. 14 presents the pressure versus angle results for the three grid generation methods. This angle refers to the centre of the cell defined by the two adjacent blades (upstream and downstream blades). From 0° to 340°, there was an overlapping of the three pressure traces: after the intake process at 74° (the corresponding upstream blade at 48°), the working fluid over-expanded from 5.4 to 1.6 bar and, between 154° (the corresponding downstream blade at 180°) and 180°, was recompressed to the average outlet pressure of 3.2 bar. From 340° to 360°, all meshing approaches showed pressure spikes due to the low and decreasing cell volumes. Unlike the rest of the cycle, the peak pressure values resulting from the three methods presented some differences. More specifically, the pressure peaks for ICEM, analytical and differential results were 7.7, 7.6 and 8.5 bar, respectively. These disagreements are due to the different treatment of the blade side wall introduced in order to maintain the specified tip clearance gap, as shown in Fig. 15. Indeed, unlike the ICEM method that successfully discretised the actual geometry (Fig. 15a), a small geometrical simplification was introduced to convert the blade side wall into a short segment on the rotor surface for the analytical method (Fig. 15b) and differential method (Fig. 15c) at the tangency region between rotor and stator. This structural simplification in the analytical method, which is relatedly smaller than that in the differential method, is closer to the real geometric shape.

The very good comparison between the benchmark (ICEM) and the analytical results confirms the accuracy of the analytical method and how this has improved previous research efforts. Moreover, given the very low cell volumes corresponding to the angular range where the pressure peaks occur, despite the mismtaching, the impact on the expander power is marginal. In fact, the torque values for analytical, ICEM and differential approaches are 0.70, 0.69 and 0.67 Nm, respectively. Hence, this comparison established the validity of the geometrical simplification.

6.2. Blade tip leakage

Leakage flows at the clearance gaps between blade tips and stator have a significant impact on the volumetric performance of vane machines. To assess the magnitude of this phenomenon, an iso clip plane was used to monitor the instantaneous blade tip leakage mass flow rate. As shown in Fig. 16, the plane was orthogonal to the throat of the nozzle resulting from the blade tip profile and the stator surface. In order to monitor the tip leakage mass flow rate, a post-processing script coded in ANSYS CFD-Post was developed to reposition the monitoring plane
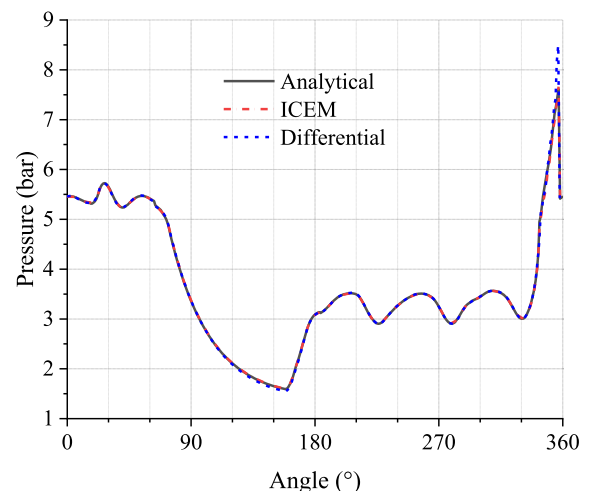

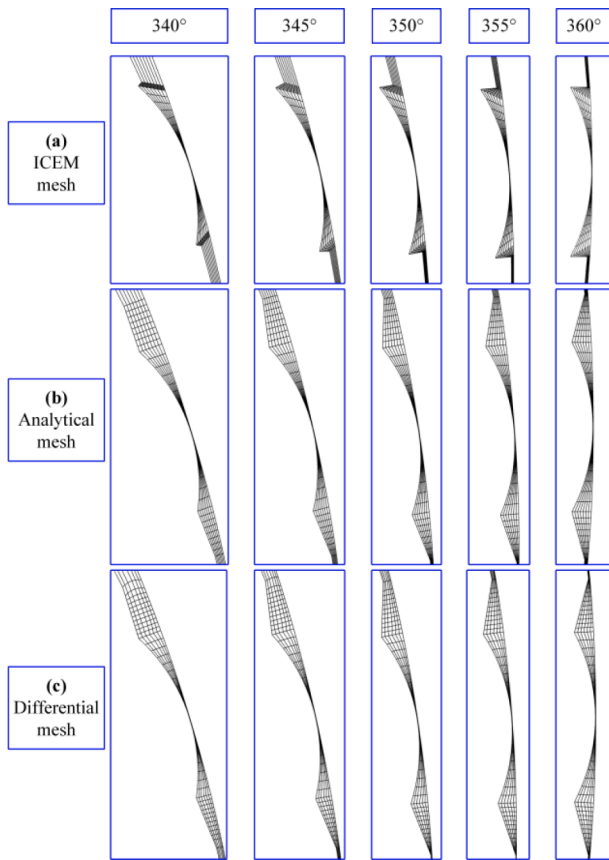**Fig. 14.** Internal pressure trace of the expander with different rotor meshing methods.

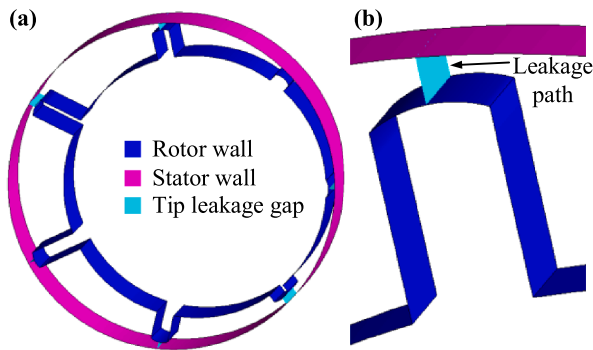**Fig. 15.** Grid comparison at the tangency region (from 340° to 360°).

Fig. 16. Post-processing setup for blade tip leakage flows evaluation: positioning of monitoring planes (a) and detail in the blade tip region (b).

during the rotation of the rotor domain at every time step.

Figure 17a shows the post-processing results with respect to a 10 μm tip clearance gap for the three grid generation approaches while Fig. 17b reports the angular evolution of the tip leakage flows for different gaps and with reference to the analytical method. As with Fig. 14, the angle in Fig. 17 also refers to the centre of the cell between the two adjacent blades, while the tip leakage rates refer to the upstream blade. The tip leakage flow mainly depends on the differential pressure across the cells that a given blade separates.

With reference to the pressure traces in Fig. 14, from 0° to 26° (the corresponding upstream blade moved along the tangency region from 334° to 360°), the cell differential pressure was negative, i.e., the pressure in the downstream cell was higher than the upstream one. This led to negative values of the leakage flows, i.e., the flow direction was opposite to the revolution speed. The pressure spikes even resulted in a
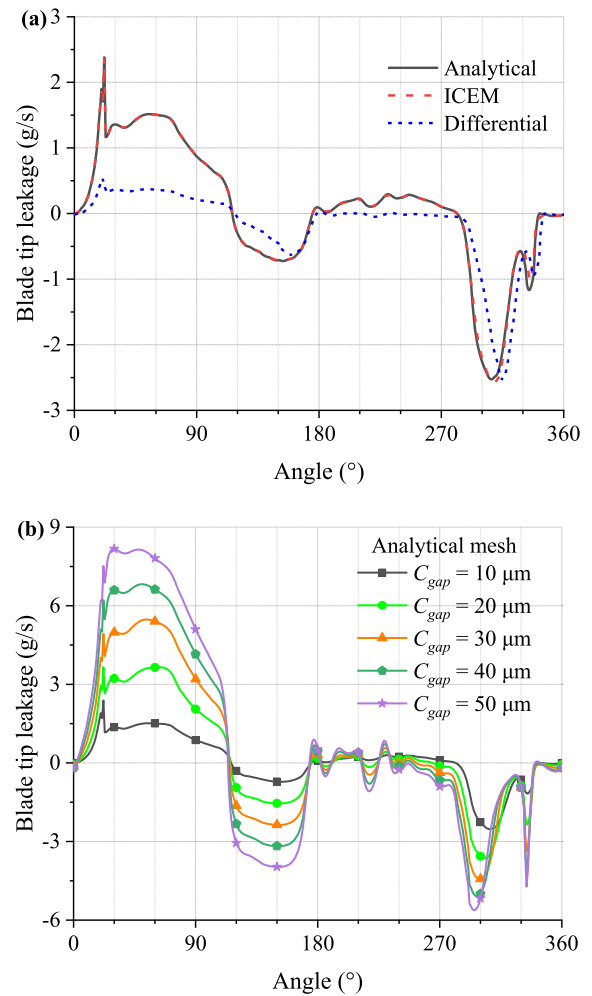

Fig. 17. Evolution of the mass flow rate at the blade tip with different rotor meshing methods (a) and different tip gap size (b).

sudden change of the leakage flows. After that, the filling process of the cell led to an increase of the leakage flow from negative to positive values. As the blade moved away from the suction port at 74° (the upstream blade at 48°), there was a sharp decrease of the leakage rate. During the expansion process between 74° (the upstream blade at 48°) to 154° (the downstream blade at 180°), leakage flow remained positive due to the positive pressure difference. After 154° (the downstream blade at 180°), the cell started to connect to the outlet port, and the recompression process led to negative pressure difference, which corresponded a decrease of the tip leakage from positive to negative values. At 206° (the upstream blade at 180°), the pressure difference disappeared. Therefore, the leakage rate increased from negative values to positive values. From 294° (the downstream blade at 320°) to 360°, the downstream cell pressure increased to a high value, leading to negative pressure difference and the resultant negative tip leakage rate.

As shown in Fig. 17a, while the analytical and ICEM results were in very good agreement, the differential ones showed lower leakages except for the first 30° and last 45°. The cycle averaged leakage flows were 0.08 g/s for the ICEM and analytical results and -0.17 g/s for the differential ones. These differences are due to the deformation of the blade tip profile introduced in order to maintain the specified clearance size for the differential approach. The very satisfactory comparison between the ICEM and analytical leakage results further validated the reliability of the newly developed method. Moreover, unlike the ICEM meshing that is a manual process and cannot be fully parameterised, the analytical one has been automated to significantly expedite the grid

generation step. For instance, to generate 360 rotor grids for this research paper, the ICEM meshing required 48 hours while the analytical one 111 seconds.

The evolution of the leakage mass flow rate at the blade tip with different tip gap size using analtical approach is given in Fig. 17b. The curves show similar angular trends, with larger tip clearance gaps resulting in higher leakage flows, as expected. It shows that the tip leakage flows are proportional with the tip gap. It can be concluded that the tip gap size has little effect on the cell pressure within the range of the tip gap from 10 to 50 μm. In other words, the upstream and the downstream pressures across the vane tip are almost constant under the conditions of this paper. Elaboration of these results is presented in the next section 6.3.

6.3. Volumetric performance

As with volumetric efficiency for pumps and compressors, the volumetric performance of expanders can be represented by the filling factor [43]. This filling factor is defined as the ratio of the measured mass flow rate to the theoretical mass flow rate displaced by the expander, where the measured values refer to the simulated results here. Fig. 18 shows the mass flow rate and filling factor of the standard expander (no supercharged inlet) with different blade tip clearance size. Both mass flow rate and filling factor were be expected to increase with the tip clearance size due to larger internal leakage flows across the blade tip [6]. The mass in the cell between the two adjacent blades grew after the intake port closing. This was due to the fact that it was fed by the leakages from surrounding cells [44]. Actually, leakage occurs on the blade tip clearance, the end face clearance, the clearance between rotor and stator, etc. Only the blade tip leakage was considered in this work. As shown in Fig. 18, both mass flow rate and filling factor are directly proportional to the tip clearance gap. Every 10 μm of the blade tip clearance led to a 1.66 g/s increase of the mass flow rate and a 0.06 increase of the filling factor.

7. Conclusions

This work proposed an innovative grid generation methodology for CFD simulations in sliding vane rotary machines that further enables the investigation of machines with multiple acting chambers, non-circular stator profiles, blade offset arrangements and asymmetric blade tip profiles. A series of analytical formulations were developed to carry out the grid boundary generation and discretisation as well as the interior node distribution, leading to a 'O' grid topology of the rotor fluid domain. The stretching functions both on blade side walls and the stator wall segments were introduced to improve mesh quality. A preliminary sensitivity analysis showed that node number and radial divisions of the blade tip are the grid generation parameters that mostly affect the mesh quality.

With reference to a vane expander test case for Organic Rankine Cycle (ORC) heat to power applications, successful experimental validation of the methodology was achieved. The simulated cell pressure results were in a 4.3% confidence interval with respect to the experimental indicating pressure data. Simulations did not consider the leakage gaps at the end walls or the blade slots and, in turn, under-predicted mass flow rate and torque.

A comparison between the proposed methodology with the manual meshing approach available in the ANSYS ICEM commercial software and a previously developed user defined nodal displacement differential grid generation method was carried out. Even if the ICEM grids benefit from no geometrical simplification at the tangency region between stator and rotor, the analytical methodology led to analogous cell pressure, torque and leakage flow results. Moreover, the analytical generation of 360 rotor grids took 111 seconds rather than 48 hours.

The leakage flow results were retrieved thanks to a novel post-processing routine based on an ANSYS CFD-Post script file that
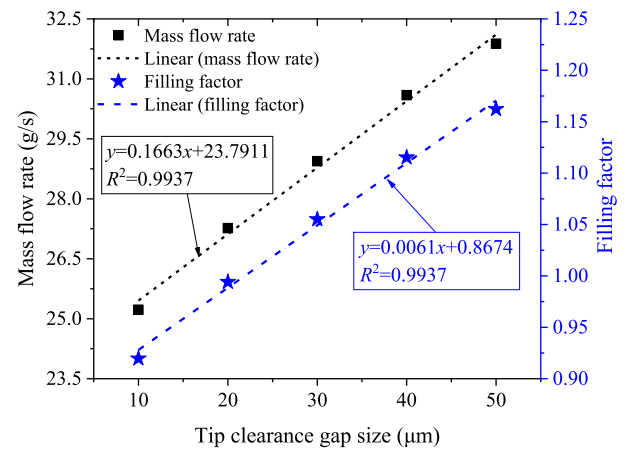

Fig. 18. Mass flow rate and filling factor with different tip clearance gap size.

computes the leakage flows between the blade tip and stator surface at every vane position. A sensitivity study referred to the ORC expander showed that every 10 μm of blade tip clearance led to an increase of 1.66 g/s in mass flow rate and a 6% increase of the filling factor.

CRediT author statement

Fanghua Ye: Methodology, Software, Formal analysis, Writing, Visualisation, Funding acquisition; **Giuseppe Bianchi:** Conceptualisation, Methodology, Formal analysis, Writing, Supervision, Project administration; **Sham Rane:** Methodology, Software, Formal analysis, Writing, Supervision; **Savvas A. Tassou:** Resources, Writing, Supervision, Project administration, Funding acquisition; **Jianqiang Deng**: Writing, Supervision, Funding acquisition.

Declaration of Competing Interest

The authors declare that they have no known competing financial interests or personal relationships that could have appeared to influence the work reported in this paper.

Acknowledgement

References

[1] Kolasiński P. Application of the multi-vane expanders in ORC systems—a review on the experimental and modeling research activities. Energies 2019;12:2975. https://doi.org/10.3390/en12152975.

[2] Yin X, Cao F, Wang J, Fang J, Wang X. Experimental investigations on the working performance of a sliding vane pump in the electronic direct cooling system. Science and Technology for the Built Environment 2020;26:484–91. https://doi.org/10.1080/23744731.2020.1712947.

[3] Sung T, Lee D, Kim HS, Kim J. Development of a novel meso-scale vapor compression refrigeration system (mVCRS). Appl Therm Eng 2014;66:453–63. https://doi.org/10.1016/j.applthermaleng.2014.02.037.

[4] Valenti G, Murgia S, Contaldi G, Valenti A. Experimental evidence of the thermal effect of lubricating oil sprayed in sliding-vane air compressors. Case Studies in Thermal Engineering 2014;4:113–7. https://doi.org/10.1016/j.csite.2014.08.001.

[5] Shouman A, Hussin AED, Hamed A, Din MSE, Mahmoud N, Baz AE. Performance evaluation of a novel dual vane rotary compressor. IOP Conference Series: Materials Science and Engineering 2017;232:012060. https://doi.org/10.1088/1757-899x/232/1/012060.

[6] Vodicka V, Novotny V, Zeleny Z, Mascuch J, Kolovratnik M. Theoretical and experimental investigations on the radial and axial leakages within a rotary vane expander. Energy 2019;189:116097. https://doi.org/10.1016/j.energy.2019.116097.

[7] Fatigati F, Bartolomeo MD, Battista DD, Cipollone R. A dual-intake-port technology as a design option for a sliding vane rotary expander of small-scale ORC-based power units. Energy Convers Manage 2020;209:112646. https://doi.org/10.1016/j.enconman.2020.112646.

[8] OM Al-Hawaj. Theoretical analysis of sliding vane energy recovery device. Desalination and Water Treatment 2012;36:354–62. https://doi.org/10.5004/dwt.2011.2639.

[9] Ye F, Deng J, Liu K, Cao Z. Performance study of a rotary vane pressure exchanger for SWRO. Desalination and Water Treatment. 2017;89:36-46. 10.5004/dwt.2017.21347.

[10] Hieronymus T, Lobsinger T, Brenner G. Investigation of the internal displacement chamber pressure of a rotary vane pump. Energies 2020;13:3341. https://doi.org/10.3390/en13133341.

[11] Lobsinger T, Hieronymus T, Brenner G. A CFD investigation of a 2D balanced vane pump focusing on leakage flows and multiphase flow characteristics. Energies 2020;13:3314. https://doi.org/10.3390/en13133314.

[12] Yan D, Kovacevic A, Tang Q, Rane S. Numerical investigation of flow characteristics in twin-screw pump under cavitating conditions. IOP Conference Series: Materials Science and Engineering 2017;232:012026. https://doi.org/10.1088/1757-899x/232/1/012026.

[13] Battara M, Mucchi E. On the relation between vane geometry and theoretical flow ripple in balanced vane pumps. Mechanism and Machine Theory 2020;146:103736. https://doi.org/10.1016/j.mechmachtheory.2019.103736.

[14] Bianchi G, Fatigati F, Murgia S, Cipollone R. Design and analysis of a sliding vane pump for waste heat to power conversion systems using organic fluids. Appl Therm Eng 2017;124:1038–48. https://doi.org/10.1016/j.applthermaleng.2017.06.083.

[15] Fatigati F, Bianchi G, Cipollonea R. Development and numerical modelling of a supercharging technique for positive displacement expanders. Appl Therm Eng 2018;140:9. https://doi.org/10.1016/j.applthermaleng.2018.05.046.

[16] Huang YM, Tsay SN. Mechanical Efficiency Optimization of a Sliding Vane Rotary Compressor. Journal of Pressure Vessel Technology 2009;131:061601. https://doi.org/10.1115/1.4000195.

[17] Bianchi G, Fatigati F, Murgia S, Cipollone R, Contaldi G. Modeling and Experimental Activities on a Small-scale Sliding Vane Pump for ORC-based Waste heat Recovery Applications. Energy Procedia 2016;101:1240–7. https://doi.org/10.1016/j.egypro.2016.11.139.

[18] Ye F, Deng J, Cao Z, Liu K. Study of energy recovery efficiency in a sliding vane pressure exchanger for a SWRO system. Desalination and Water Treatment 2018;119:10. https://doi.org/10.5004/dwt.2018.22059.

[19] Yang B, Peng X, He Z, Guo B, Xing Z. Experimental investigation on the internal working process of a CO2 rotary vane expander. Appl Therm Eng 2009;29:2289–96. https://doi.org/10.1016/j.applthermaleng.2008.11.023.

[20] Yang B, Peng X, Sun S, Guo B, Xing Z. A study of the vane dynamics in a rotary vane expander for the transcritical CO2 refrigeration cycle. Proceedings of the Institution of Mechanical Engineers, Part A: Journal of Power and Energy 2009;223:429–40. https://doi.org/10.1243/09576509jpe698.

[21] Murgia S, Valenti G, Colletta D, Costanzo I, Contaldi G. Experimental investigation into an ORC-based low-grade energy recovery system equipped with sliding-vane expander using hot oil from an air compressor as thermal source. Energy Procedia 2017;129:339–46. https://doi.org/10.1016/j.egypro.2017.09.204.

[22] Bianchi G, Cipollone R. Friction power modeling and measurements in sliding vane rotary compressors. Appl Therm Eng 2015;84:276–85. https://doi.org/10.1016/j.applthermaleng.2015.01.080.

[23] Lu Y, Zhao Y, Bu G, Shu P. The integration of water vane pump and hydraulic vane motor for a small desalination system. Desalination 2011;276:60–5. https://doi.org/10.1016/j.desal.2011.03.023.

[24] Bianchi G, Rane S, Fatigati F, Cipollone R, Kovacevic A. Numerical CFD Simulations and Indicated Pressure Measurements on a Sliding Vane Expander for Heat to Power Conversion Applications. Designs 2019;3:31. https://doi.org/10.3390/designs3030031.

[25] Gu H, Chen Y, Wu J, Jiang Y, Sundén B. Impact of discharge port configurations on the performance of sliding vane rotary compressors with a rotating cylinder. Appl Therm Eng 2021;186:116526. https://doi.org/10.1016/j.applthermaleng.2020.116526.

[26] Rane S, Kovacevic A, Stosic N, Kethidi M. Grid deformation strategies for CFD analysis of screw compressors. International Journal of Refrigeration 2013;36:1883–93. https://doi.org/10.1016/j.ijrefrig.2013.04.008.

[27] Spille-Kohoff A, Hesse J, Andres R, Hetze F. CFD simulation of a dry scroll vacuum pump with clearances, solid heating and thermal deformation. IOP Conference Series: Materials Science and Engineering 2017;232:012052. https://doi.org/10.1088/1757-899x/232/1/012052.

[28] Spille-Kohoff A, Hesse J, Shorbagy AE. CFD simulation of a screw compressor including leakage flows and rotor heating. IOP Conference Series: Materials Science and Engineering 2015;90:012009. https://doi.org/10.1088/1757-899x/90/1/012009.

[29] Zhang JW, Wu YR, Hsieh SH, Huang CS. Use of CFD to investigate flow characteristics and oil distribution inside an oil-injected screw compressor. IOP Conference Series: Materials Science and Engineering 2019;604:012016. https://doi.org/10.1088/1757-899x/604/1/012016.

[30] Song L, Zeng L, Zhou J, Luo X. Profile design for the cylinder of a double-acting rotary vane compressor. Proceedings of the Institution of Mechanical Engineers, Part C: Journal of Mechanical Engineering Science 2015;230:2300–13. https://doi.org/10.1177/0954406215592923.

[31] Hu YS, Wei HJ, Xu J, Wan PK, Wu F, Luo FY, et al. A theoretical study on the novel structure of vane compressor for high efficiency. IOP Conference Series: Materials Science and Engineering 2019;604:012067. https://doi.org/10.1088/1757-899x/604/1/012067.

[32] Bianchi G, Rane S, Kovacevic A, Cipollone R. Deforming grid generation for numerical simulations of fluid dynamics in sliding vane rotary machines. Advances in Engineering Software 2017;112:180–91. https://doi.org/10.1016/j.advengsoft.2017.05.010.

[33] Bianchi G, Rane S, Kovacevic A, Cipollone R, Murgia S, Contaldi G. Numerical CFD simulations on a small-scale ORC expander using a customized grid generation methodology. Energy Procedia 2017;129:843–50. https://doi.org/10.1016/j.egypro.2017.09.199.

[34] Montenegro G, Torre AD, Fiocco M, Onorati A, Benatzky C, Schlager G. Evaluating the performance of a rotary vane expander for small scale organic rankine cycles using CFD tools. Energy Procedia 2014;45:1136–45. https://doi.org/10.1016/j.egypro.2014.01.119.

[35] Rak J, Błasiak P, Kolasiński P. Influence of the Applied Working Fluid and the Arrangement of the Steering Edges on Multi-Vane Expander Performance in Micro ORC System. Energies 2018;11. https://doi.org/10.3390/en11040892.

[36] Ye F, Deng J, Liu K. CFD simulation on cavitation in a rotary vane energy recovery device. Energy Procedia 2019;158:4785–90. https://doi.org/10.1016/j.egypro.2019.01.720.

[37] Battara M, Blum A, Mucchi E. Kinematics of a balanced vane pump with circular tip vanes. Mechanism and Machine Theory 2019;137:355–73. https://doi.org/10.1016/j.mechmachtheory.2019.03.034.

[38] Basha N, Kovacevic A, Rane S. User defined nodal displacement of numerical mesh for analysis of screw machines in FLUENT. IOP Conference Series: Materials Science and Engineering 2019;604:012012. https://doi.org/10.1088/1757-899x/604/1/012012.

[39] Rane S, Kovačević A, Stošić N, Smith I. Analysis of real gas equation of state for CFD modelling of twin screw expanders with R245fa, R290, R1336mzz(Z) and R1233zd(E). International Journal of Refrigeration 2021;121:313–26. https://doi.org/10.1016/j.ijrefrig.2020.10.022.

[40] Bao J, Zhao L. A review of working fluid and expander selections for organic rankine cycle. Renewable and Sustainable Energy Reviews 2013;24:325–42. https://doi.org/10.1016/j.rser.2013.03.040.

[41] Imran M, Usman M, Park BS, Lee DH. Volumetric expanders for low grade heat and waste heat recovery applications. Renewable and Sustainable Energy Reviews 2016;57:1090–109. https://doi.org/10.1016/j.rser.2015.12.139.

[42] Rane S, Kovačević A. Application of numerical grid generation for improved CFD analysis of multiphase screw machines. IOP Conference Series: Materials Science and Engineering 2017;232:012017. https://doi.org/10.1088/1757-899x/232/1/012017.

[43] Kishizawa N, Tsuzuki K, Hayatsu M. Low pressure multi-stage RO system developed in "Mega-ton Water System" for large-scaled SWRO plant. Desalination 2015;368:81–8. https://doi.org/10.1016/j.desal.2015.01.045.

[44] Fatigati F, Di Bartolomeo M, Cipollone R. On the effects of leakages in Sliding Rotary Vane Expanders. Energy 2020;192:116721. https://doi.org/10.1016/j.energy.2019.116721.